Supplementary Information

Observation of Nanotwinning and Room Temperature Ferromagnetism in Sub – 5 nm BiFeO₃ Nanoparticles: A Combined Experimental and Theoretical Study

Mandar M. Shirolkar[1], Xiaolei Dong, Jieni Li, Shiliu Yin, Ming Li and Haiqian Wang*

Hefei National Laboratory for Physical Sciences at the Microscale, University of Science and Technology of China, Hefei, Anhui 230026, People's Republic of China

*Corresponding Author**: hqwang@ustc.edu.cn
mandar@ustc.edu.cn; mmshirolkar@gmail.com**

Crystal Structure and morphology measuements on BiFeO₃ bulk particles
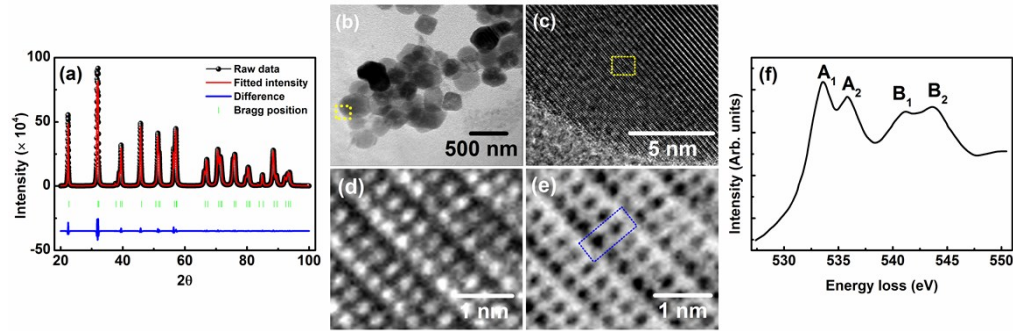
Figure S1 (a) Rietveld refined X – ray diffraction of BiFeO₃ bulk particles. (b) TEM micrograph of as prepared BiFeO₃ bulk particles. (c) HRTEM of highlighted (with yellow square in (b)) BiFeO₃ particle. (d) HRTEM of selected region of (c). (e) O K – edge EELS map of (d). (f) O K – edge EELS spectrum acquired on highlighted region of (e).

- XRD shows that as prepared BiFeO₃ particles exhibit high purity and $R3c$ symmetry (Figure S1(a)). The structural parameters obtained from the refinement are as follows: (i) lattice parameters: a = 5.5182 Å and c = 13.7145 Å and (ii) atomic coordinates: Bi(0, 0, 0), Fe(0, 0, 0.22) and O(0.453, 0.0265, 0.96).

- The average particle size was observed to be 500 ± 10 nm (Figure S1(b) – (e)).

- The sharp EELS features reveals that Bi – O – Fe coordination in bulk BiFeO₃ is strong (Figure S1(f)) compared to nanodimension.

HRTEM Analysis: The subscript 'F' in the following HRTEM micrographs represent filtered image.
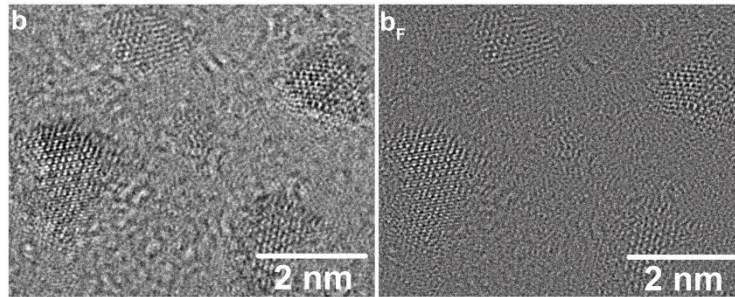
Figure S2 HRTEM and corresponding FFT filtered (b_F) image of BFO NPs below 2 nm size.
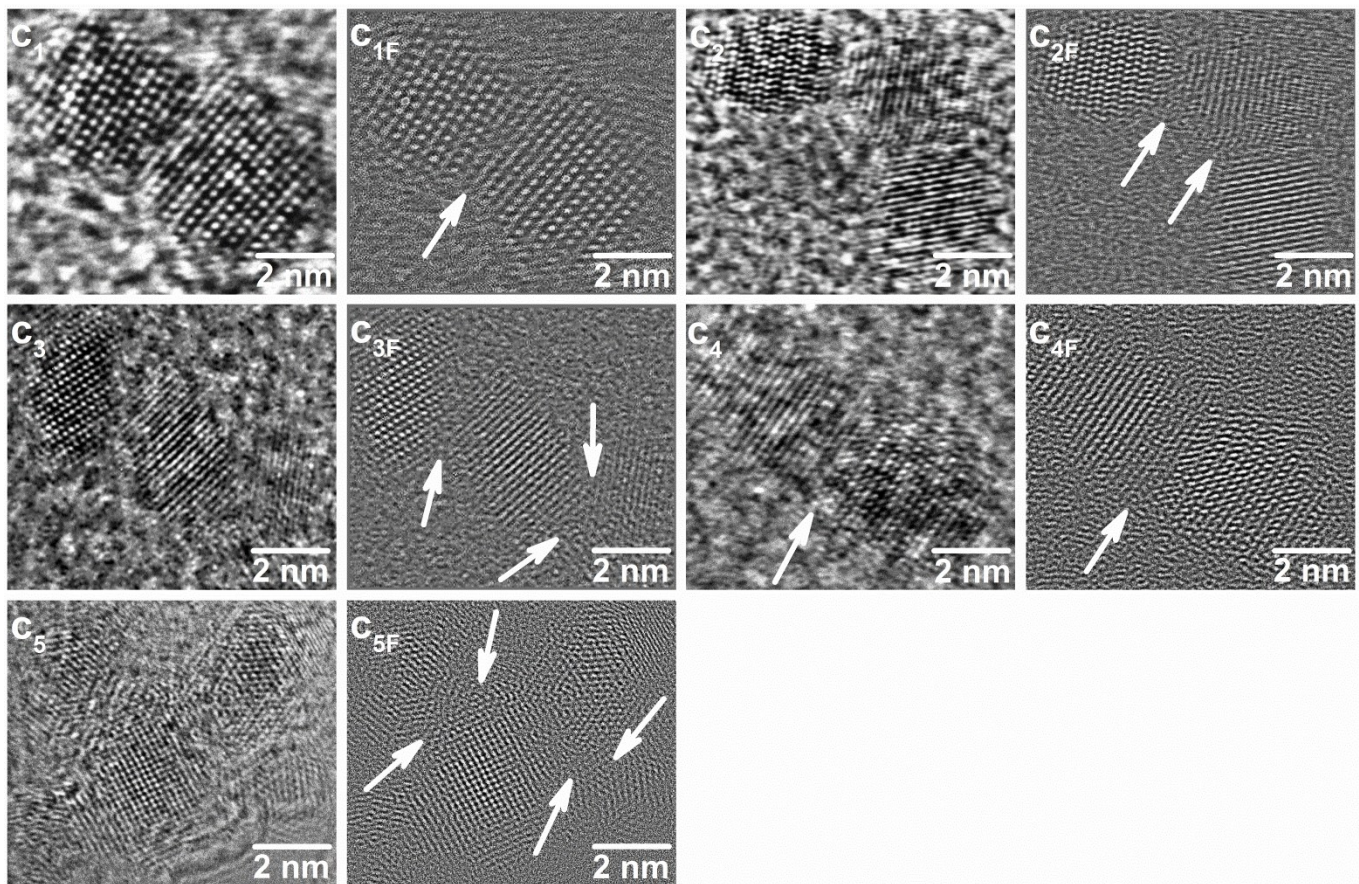
Figure S3 HRTEM Micrographs and FFT filtered images of corresponding micrograph.The dislocations and defects are shown with white colored arrows.
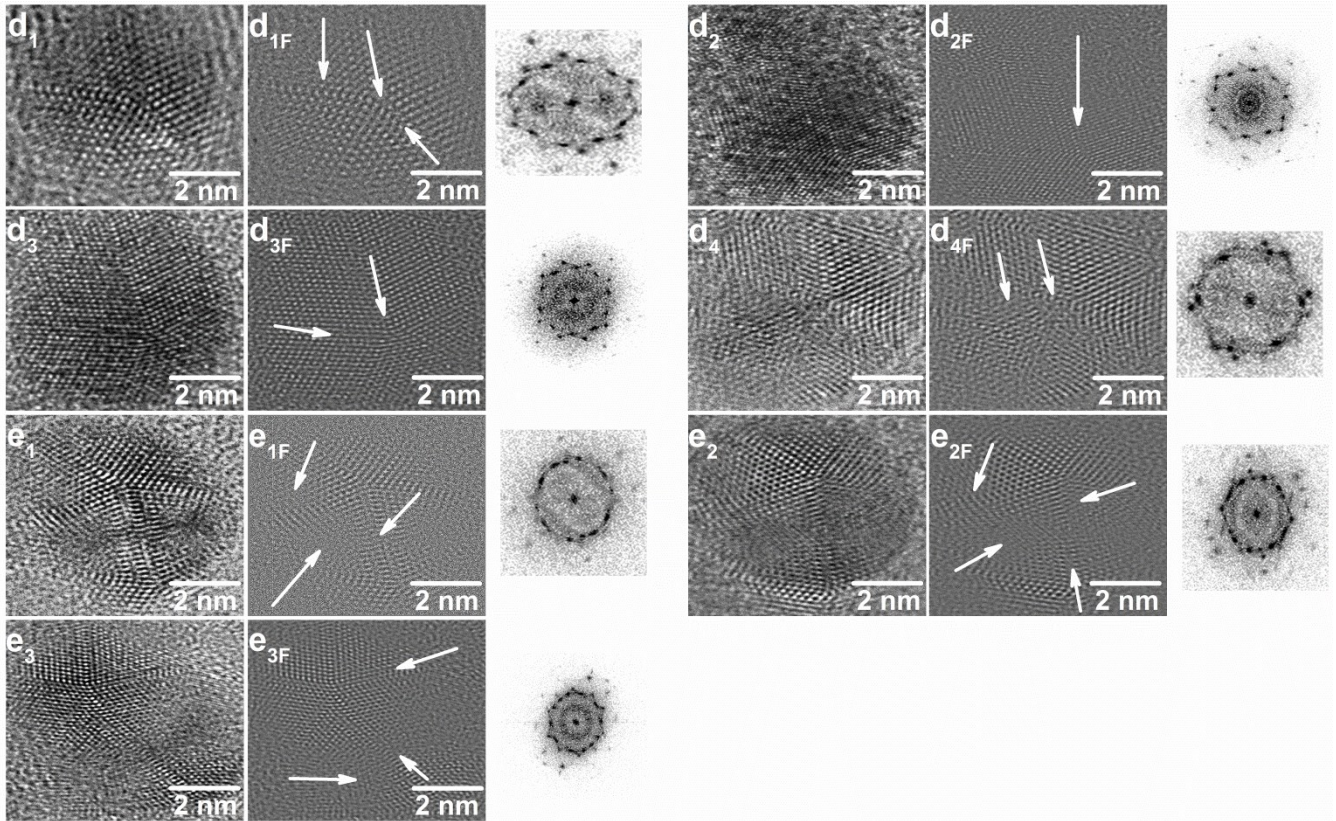
Figure S4 HRTEM micrographs, corresponding FFT filtered images and FFT of nanotwinned BiFeO$_3$ nanoparticles. The dislocations and defects are indicated with white colored arrows.
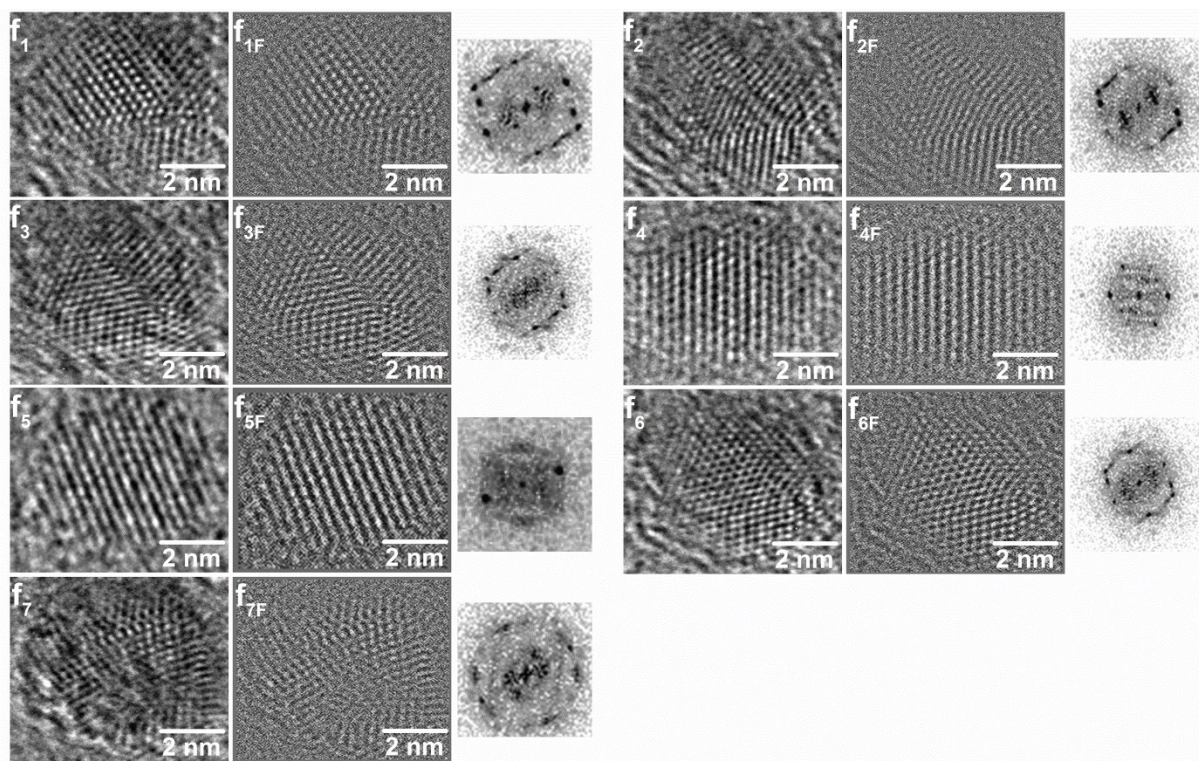
Figure S5 HRTEM micrographs, corresponding FFT filtered images and FFT of spherical BiFeO$_3$ nanoparticles.
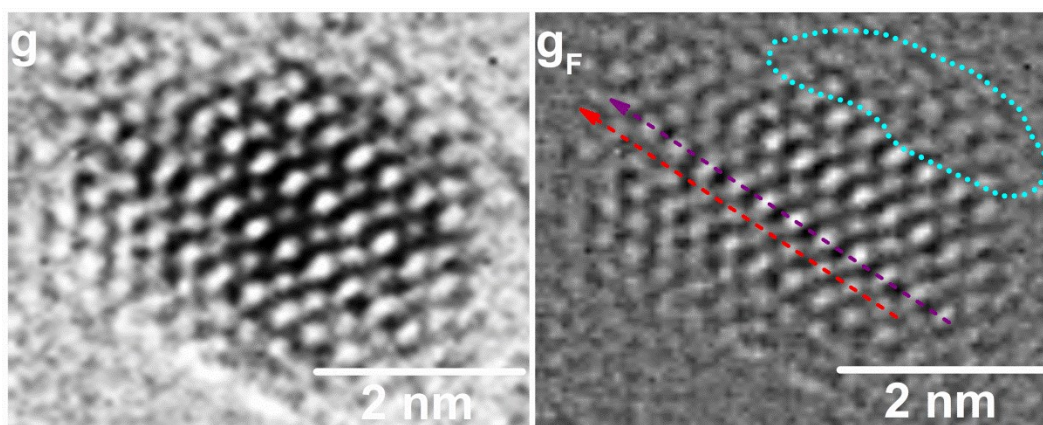
Figure S6 HRTEM micrograph and FFT filtered image of the single BiFeO$_3$ nanoparticle. The iron atom column is represented with red color dotted arrow and bismuth atom column is represented with the violet color dotted arrow. The defects in the nanoparticle are illustrated with a cyan color dotted line.

Elemental analysis of BiFeO₃ Nanoparticles
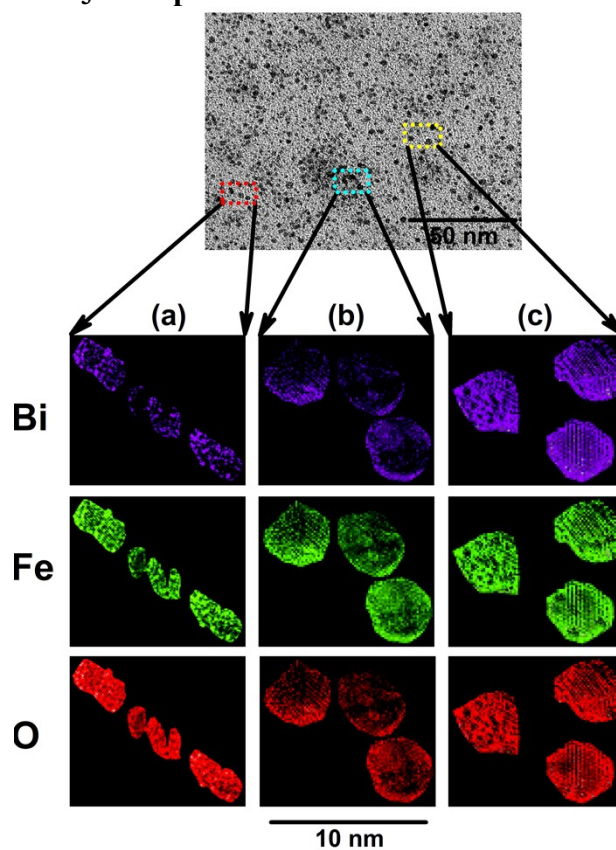
Figure S7 Elemental composition maps of selected BiFeO$_3$ sub – 5 nm nanoparticles (of Figure 1). (a) represents EDS mapping on the particles (c$_1$), (c$_2$) and (c$_3$), (b) shows EDS mapping on the NPs (d$_1$), (e$_1$) and (e$_2$) and (c) EDS of (f$_1$), (f$_4$) and (f$_7$) NPs.

Comparison of EELS O K – edge scan for sub – 5nm nanoparticles and bulk BiFeO$_3$
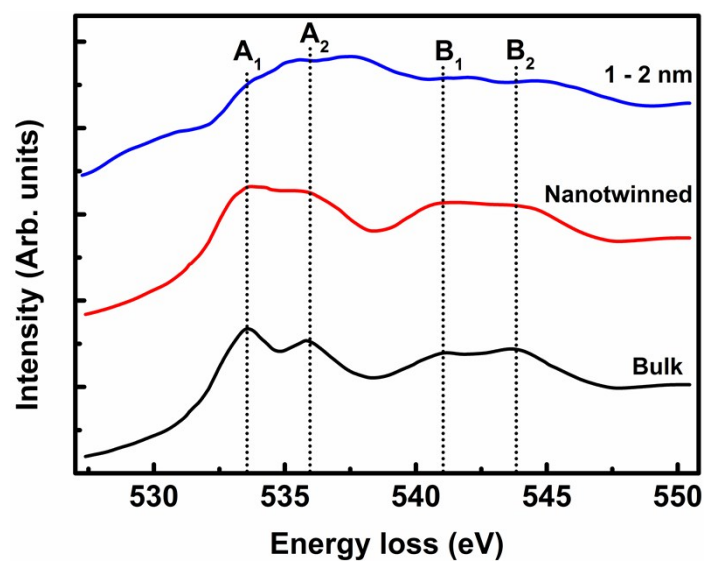
Figure S8 EELS O K – edge scan for sub – 5 nm nanoparticles and bulk BiFeO$_3$ particles.

Theoretical prediction of nanotwinning and quasi – crystal nature

We now discuss the nanotwinning and quasi – crystal symmetry nature observed in the HRTEM studies (Fig. 1). We note that these structures were observed in the specific size regime of BFO NPs (2 – 4 nm). Several researchers have identified the similar structures in case of other nanoparticles and mainly reported due to (i) crystal symmetry, (ii) periodic reversal of atomic stacking order, (iii) grain size, (iv) anisotropy in the surface energy and (v) coalescence of nanograins either through the preferential attachment of facets or the ordered combination of suitably oriented two or more nanograins[1-4]. In BFO, at sub – 5 nm dimension the above mentioned mechanisms could have occurred simultaneously, which enables the formation of twinning and quasi – crystals. We explained it in the following way. In general, $BiFeO_3$ crystallizes in a rhombohedral perovskite structure with space group $R3c$ (a_{rh} = 3.965 Å and $\alpha_{rh} \approx$ 89.3° – 89.4° ($\alpha_{rh(average)}$: 89.35°) and the (110) plane had lowest surface energy[5]. In BFO lattice oxygen atoms are twisted around the [111] direction[5]. The rhombohedral structure of BFO can be described in a hexagonal frame of reference in terms of a pseudocubic (pc) unit cell $[001]_{hexagonal} \parallel [111]_{pseudocubic}$ ($a_{pc} \approx$ 5.899Å and $\alpha_{pc} \approx$ 70.85°, calculated considering $\alpha_{rh} \approx$ 89.35°)[5, 6]. The rhombohedral phase is likely to be formed by a compression of the cubic unit cell (ideal) along one of the four body diagonals in <111> direction, which gives four different rhombohedral variants. A combinations of any two variants form one twin structure. It results in four different domain states, forming $(100)_{pc}$ or $(110)_{pc}$ twin planes. Additionally, in BFO the variation in O – Fe – O bond angle and Fe – O bond length gives distortion in FeO_6 octahedra, which leads to the rhombohedral distortion. The rhombohedral distortion affects Goldschmidt tolerance factor $G = d_{Bi-O}/\sqrt{2}d_{Fe-O}$. The G factor also corresponds to a rotation of the FeO_6 octahedra (ω), which is in the range 11 – 14° ($\omega_{(average)}$ = 13.5°) around the $[111]_{pc}$ direction,

which reduces the symmetry from cubic to rhombohedral[5]. The twin planes can be observed in the $BiFeO_3$ in the ultrathin epitaxial films or with the decrease in the particle size beyond a certain limit[7]. In the present case, decrease in the particle size directly affects the G factor and hence ω, a_{pc} and α_{pc}. It leads to the formation of individual nanograins with twin planes. The anisotropy in surface energy of the twin plane leads to the coalescence of BFO nanograins with the facets {110}. We note that not all facets are suitable for the coalescence and the attachment of nanograins can occur only on {110} planes and there is no nanograin attached to {100} plane. Hence, the preferential attachment of the planes give nanotwinning and quasi crystal features to sub – 5 nm BFO NPs. The coalescence of nanograins is governed by an intrinsic stacking fault. We observed two types of coalescence, (i) coalescence of two or more nanograins, which yields attachment of BFO nanograins and (ii) the preferential attachment of facets of the nanograins, which gives twinning of multiple BFO nanograins resulting in the quasi crystal structures. During the coalescence, variations in the twinning angle give significant strain induced dislocations and other structural defects.

Comparison of Raman spectra: BiFeO₃ sub – 5 nm nanoparticles and bulk particles
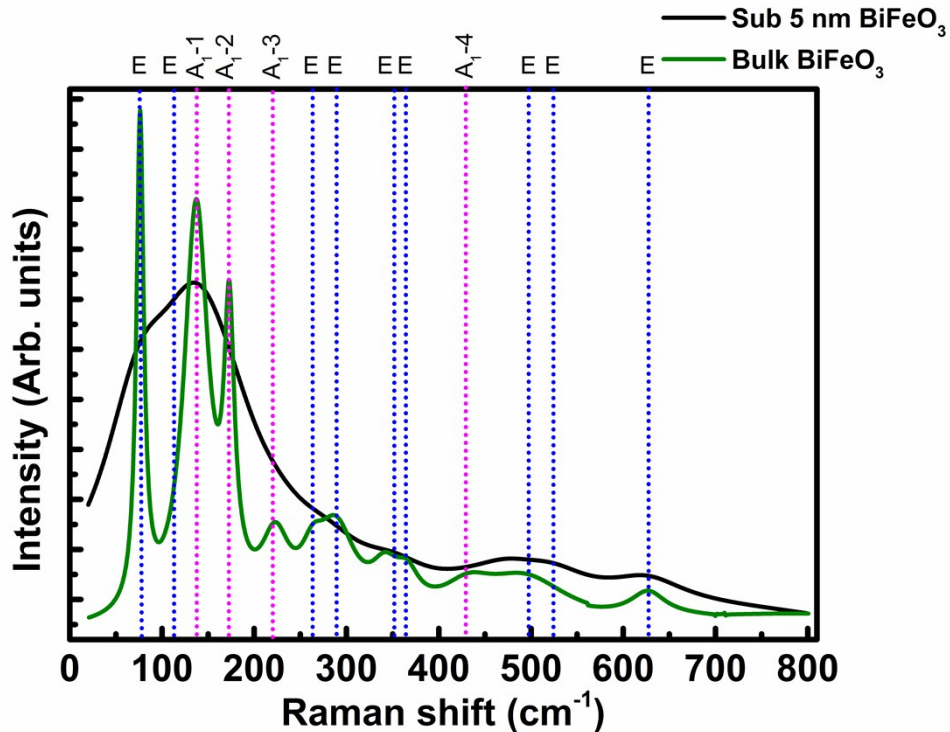
Figure S9 Comparative study of Raman spectra for sub – 5 nm BiFeO₃ nanoparticles and bulk BiFeO₃ particles.

Table T1 A comparative study of Raman modes observed for sub – 5 nm nanoparticles and bulk BiFeO₃ particles.

Raman modes	Raman shift (cm^{-1})	
	BiFeO₃ NPs Sub – 5 nm	BiFeO₃ bulk 500 ± 10 nm
A_1-1	138	144
A_1-2	172	176
A_1-3	221	226
A_1-4	428	434
E	62	78
E	100	129
E	262	284
E	291	293
E	339	357
E	361	375
E	473	476
E	522	529
E	621	632

XPS analysis

10

X – ray photoelectron spectroscopy (XPS) study on the sample was carried out using Thermo scientific ESCALAB 250 using Al Kα radiation (1486.6 eV). During the measurement, the base pressure of experimental chamber was ≈ 10^{-8} mbar. Figure S10 shows XPS measurements on BFO NPs. The survey scan (Figure. S10(a)) shows presence of Bi, Fe and O along with a small amount of C. The presence of carbon can be attributed to the sample preparation conditions. The detected carbon peak was considered for correcting the charging effect. Overall, the survey scan confirms the purity of BFO NPs. The narrow range XPS scans for Bi 4f (154 to 170 eV), Fe 2p (705 to 735 eV) and O 1s (525 to 535 eV) are shown in Figure S10(b) – (d).
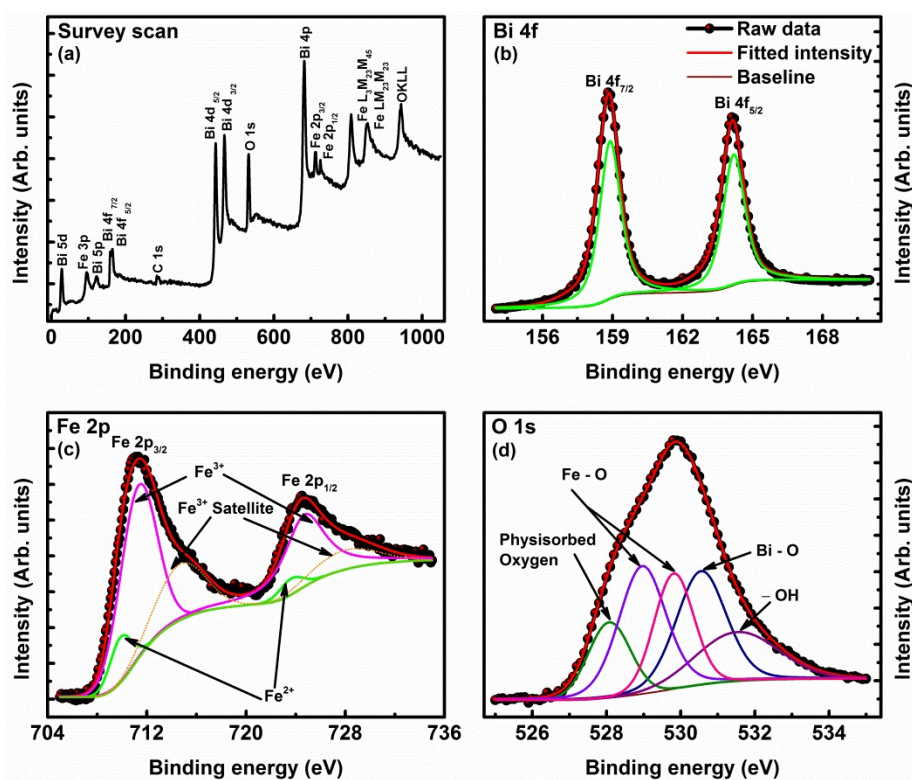
Figure S10 XPS of as prepared $BiFeO_3$ nanoparticles. (a) represents survey scan showing chemical composition of sample. (b), (c) and (d) respectively represents deconvoluated narrow scan for bismuth, iron and oxygen respectively.

Figure S10(b) shows the fitted Bi 4f narrow scan spectrum for BFO NPs. It can be seen that Bi 4f doublet consists of two peaks centered at 158.64 eV (Bi^{3+} $4f_{7/2}$) and 163.98 eV (Bi^{3+}

$4f_{5/2}$) it represent Bi – O bonds[8-10]. The spin orbit splitting energy was observed to be 5.34 eV, which is comparable with reported results for Bi 4f in case of BFO ($\Delta_{Bi\ 4f}$ = 5.31 eV).

Figure S10(c) shows deconvoluted Fe 2p narrow scan spectrum. The fitting shows that Fe 2p doublet peaks centered at 711.60 eV (Fe^{3+} $2p_{3/2}$) and 724.95 eV (Fe^{3+} $2p_{1/2}$), described the Fe – O bonds[10]. The spin orbit splitting for Fe 2p doublet was observed to be around 13.35 eV, which is also reasonably comparable with XPS analysis of Fe 2p in case of BFO ($\Delta_{Fe\ 2p}$ = 13.36 eV) and Fe_2O_3 ($\Delta_{Fe\ 2p}$ = 13.6 eV)[9, 10]. Fe 2p scan also shows subpeaks centered around 710.30 and 723.73 eV, which are mainly related to Fe – O bonds for Fe^{2+} oxidation state of iron[9, 10]. We further observed that Fe^{2+} ions are $\approx$ 15 % of the entire Fe component and can contribute to the overall multiferroic behavior of the NPs.

The fitted narrow XPS scan for O 1s is shown in Figure S10(d). It shows a broad O 1s peak centered at 529.9 eV. This broad feature composed of five subpeaks, which are mainly ascribed to physisorbed oxygen: 528.07 eV, Fe_2 – $(O\ 1s)_3$: 528.97 eV, Fe – (O 1s): 529.81 eV, Bi_2 – $(O\ 1s)_3$: 530.55 eV and surface adsorbed species: 531.52 eV. The occurrence of surface adsorbed species such as H_2O, CO_2 on the sample surface can be either from ambient air during the sol – gel process or due to the presence of oxygen vacancies[8-10].

The stoichiometry of the NPs was determined from the XPS studies. The NPs exhibit the stoichiometry $Bi_{1.0}Fe^{+3}_{0.84}Fe^{+2}_{0.16}O_{3-0.16}V_o^{\bullet}$, where $V_o^{\bullet}$ represent the oxygen vacancies present in the NPs due to particle size effects.

^{57}Fe Mössbauer spectroscopy studies on 573 K (300 ºC) and 623 K (350 ºC) annealed BiFeO$_3$ nanoparticles

Figure S11(a) and (b) shows room temperature Mössbauer spectroscopy studies on 573 K (300 ºC) and 623 K (350 ºC) annealed samples, which are observed to be partially and fairly crystalline states respectively.
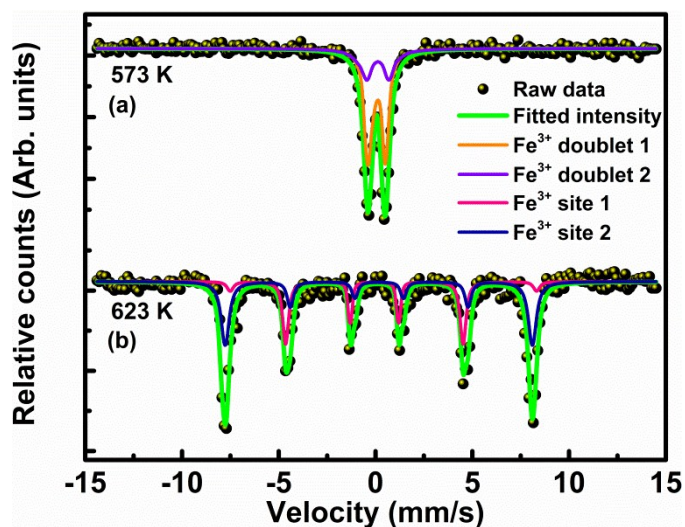
Figure S11 Room temperature Mössbauer spectroscopy studies on 573 K and 623 K annealed BFO nanoparticles.

The fitting reveals that in the proximity to 573 K, the davidite phase in BFO NPs is destroyed. The quadrupole doublet represents the presence of Fe^{3+} oxidation state of iron and indicates that quadrupole interactions are much stronger than magnetic hyperfine interactions[11]. The occurrence of doublet also shows the superparamagnetic nature of BFO nanoparticles[11]. The derived Mössbauer parameters from fitting of the data are shown in Table 1.

While, the existence of high spin ferric ions (Fe^{3+}) in BFO lattice with magnetic sextets was observed for the sample annealed at 623 K, representing that iron exists in trigonal distortion (see Figure S11(b)).

Table T2 Mössbauer parameters derived from least square fitting of the data.

Annealing Temperature (K)	Site	Isomer Shift (IS) (mm/s) ± 0.02	Quadrupole Splitting (QS) (mm/s) ± 0.04	Hyperfine Field (B_{HF}) (KOe) ± 0.05
573 **(300 °C)**	Fe^{3+} (double 1) Fe^{3+} (doublet 2)	0.36 0.44	0.54 1.90	-- --
623 **(350 °C)**	Fe^{3+} (Site 1) Fe^{3+} (Site 2)	0.42 0.40	0.78 0.71	520 501

The study reveals that Fe^{3+} exist in the two crystallographic environments and gives different electric field gradients in the octahedral environment of both Fe^{3+} sites (shown with site 1 and 2 in Figure S11(b))[12, 13]. The broadening in the sextets suggests the suppressed intrinsic spiral spin arrangement of Fe^{3+} in BFO lattice due to particle size effects[14]. Table 1 shows Mössbauer parameters extracted from the fitting of the data, which are consistent with previously reported Mössabuer parameters for BFO nanoparticles[12, 13].

References

1. T. Ling, H. Yu, X. Liu, Z. Shen and J. Zhu, *Crystal Growth & Design*, 2008, 8, 4340-4342.

2. S. Liu, Q. Zhang, Y. Li, M. Han, L. Gu, C. Nan, J. Bao and Z. Dai, *Journal of the American Chemical Society*, 2015, 137, 2820-2823.

3. Y. Q. Wang, R. Smirani and G. G. Ross, *Nano letters*, 2004, 4, 2041-2045.

4. Y. Q. Wang, R. Smirani, G. G. Ross and F. Schiettekatte, *Physical Review B*, 2005, 71.

5. G. Catalan and J. F. Scott, *Advanced materials*, 2009, 21, 2463-2485.

6. J. Silva, A. Reyes, H. Esparza, H. Camacho and L. Fuentes, *Integrated Ferroelectrics*, 2011, 126, 47-59.

7. C. J. M. Daumont, S. Farokhipoor, A. Ferri, J. C. Wojdeł, J. Íñiguez, B. J. Kooi and B. Noheda, *Physical Review B*, 2010, 81.

8. S. Chaturvedi, I. Sarkar, M. M. Shirolkar, U. S. Jeng, Y.-Q. Yeh, R. Rajendra, N. Ballav and S. Kulkarni, *Applied Physics Letters*, 2014, 105, 102910.

9. A. Tamilselvan, S. Balakumar, M. Sakar, C. Nayek, P. Murugavel and K. Saravana Kumar, *Dalton Trans*, 2014, 43, 5731-5738.

10. Z. Quan, H. Hu, S. Xu, W. Liu, G. Fang, M. Li and X. Zhao, *Journal of Sol-Gel Science and Technology*, 2008, 48, 261-266.

11. B. Babić-Stojić, V. Jokanović, D. Milivojević, Z. Jagličić, D. Makovec, N. Jović and M. Marinović-Cincović, *Journal of Nanomaterials*, 2013, 2013, 1-9.

12. M. M. Shirolkar, R. Das, T. Maity, P. Poddar and S. K. Kulkarni, *The Journal of Physical Chemistry C*, 2012, 116, 19503-19511.

13.   M. M. Shirolkar, C. Hao, X. Dong, T. Guo, L. Zhang, M. Li and H. Wang, *Nanoscale*, 2014, 6, 4735-4744.

14.   J. Landers, S. Salamon, M. Escobar Castillo, D. C. Lupascu and H. Wende, *Nano letters*, 2014, 14, 6061-6065.